Supplementary material for

"A type of novel Weyl semimetal candidates: layered transition metal monochalcogenides Mo_2XY(X, Y=S, Se, Te, X≠Y)"

Lijun Meng✉[1,2,3], Yizhi Li[1], Jiafang Wu[1], Lingling Zhao[1], Jianxin Zhong✉[1,2]

[1]Faculty of Materials and Optoelectronic Physics, Xiangtan University, Xiangtan 411105, Hunan, People's Republic of China

[2]Hunan Key Laboratory for Micro-Nano Energy Materials and Devices, Hunan, People's Republic of China

[3]Department of Physics, University of Warwick, Coventry, CV4 7AL, United Kingdom

1. The calculation methods

In first-principles based calculations, we utilized the plane-wave basis set and the projector augmented wave method, which is implemented in the Vienna *Ab initio* Simulation Package (VASP)[1]. We used the generalized gradient approximation (GGA) in the Perdew-Burke-Ernzerhof (PBE) parameterization for the exchange-correlation functional and density functional theory (DFT) in electronic band calculations [1-3]. Plane-wave cutoff energy of 600eV, a force convergence of criteria 0.001eV/Å and a Monkhorst-Pack(MP) mesh of 16×16×8 were used[4, 5]. The *k* point mesh 12×12×6 also reproduced very similar results for strain-free cases and was used in strained systems. All calculations include SOC interaction and vdW correction between interlayers which is realized by the DFT-D3 scheme[6].

To verify the thermal stability, we conducted a long-timescale first-principles molecular dynamics (FPMD) calculation based on a 4×4×2 supercell at 300K. A velocity Verlet algorithm, with time step of 2*fs* and *NVT* ensemble, was adopted. We used a plane-wave cutoff energy of 400eV, a force convergence criteria of 0.1eV/ Å and an MP mesh of 1×1×1 in supercell calculations. To confirm the dynamic stability, we performed the calculations of phonon spectrum with a plane-wave cutoff energy of 600eV, an energy convergence criteria of 1.0×10^{-8}eV and an MP mesh of 1×1×2 based on a 6×6×1 supercell. The harmonic interatomic force constants and dynamic matrices are obtained through density functional perturbation theory(DFPT), which was realized in the PHONOPY code[7].

The topological properties are identified by calculating the handedness of Weyl node, Wannier charge center (WCC) and surface Fermi arcs using Wannier-based tight-binding method [8, 9]. The tight-binding matrices were constructed by projecting the extended Bloch orbitals into maximally localized Wannier orbitals in the Wannier90 package[8]. We generated atomic-like Wannier orbitals for Mo-*d* and S/Se/Te-*p* orbitals in order to reproduce accurately the DFT-based bands in the energy window (-1.5eV, 1.5eV). We calculated surface states and the Fermi arcs on the (001) surface by considering a half-infinite surface using the iterative Green's function method[10]. The *k*-

✉ The corresponding author Email: ljmeng@xtu.edu.cn
✉ The corresponding author Email: jxzhong@xtu.edu.cn

dependent local densities of states are projected from the half-infinite bulk to the outermost surface unit cell.

2. Thermal stability and dynamic stability for Mo_2TeS and Mo_2TeSe

The time evolution of temperature and total energy per formula unit cell in FPMD calculations for Mo_2TeS and Mo_2TeSe are shown in Fig.1S (*a*) (*c*). A stable long time (up to 10*ps*) scale thermal fluctuation around average values demonstrates the thermal stability of their structures at room temperature.

Similar to Mo_2SeS, we carried out the calculations of phonon dispersions for Mo_2TeS and Mo_2TeSe to check their dynamic stability. The phonon spectra along high symmetry path M-Γ-K-H-A-Γ-L for Mo_2TeS and Mo_2TeSe are presented in Fig.1S (*b*) (*d*). The absence of negative frequency in the phonon bands illustrate that the Mo_2TeS and Mo_2TeSe are dynamically stable.

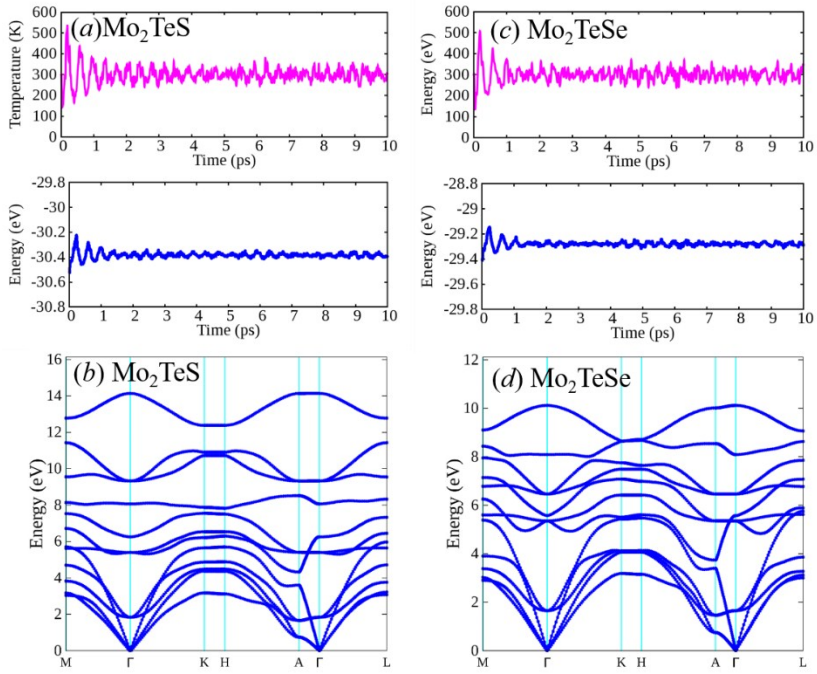

Fig.1S (Color Online). The time evolution of temperature, total energy in FPMD, and the phonon dispersions for Mo_2TeS ((*a*) (*c*)) and Mo_2TeSe ((*c*) (*d*)).

3. Orbital-resolved bands for Mo_2TeS and Mo_2TeSe

In the absence of SOC, nodal lines also form on the mirror planes by the crossings of CB and VB with opposite mirror eigenvalue for both Mo_2TeS and Mo_2TeSe, which is analogous to the Mo_2SeS. The nodal lines are related by C_{3z} rotation symmetry. After adding SOC, the orbit-resolved bands along high symmetry path M-Γ-K-H-A-Γ-L in the BZ for Mo_2TeS and Mo_2TeSe are plotted in Fig.2S. The bands near the Fermi level are mainly composed of Mo-*d* orbitals and S/Se/Te-*p* orbitals, which is similar to transition metal dichalcogenides and diphosphates(WTe_2[11], $MoTe_2$[12, 13], MoP_2, WP_2[14]). The hole-like pockets around Γ point and electron-pockets on the lines M-Γ and Γ-K at the Fermi level remain. Similar to Mo_2SeS, the two fourfold degenerate nodes at high symmetry point A split into four twofold degenerate points when SOC turns on. The

addition of SOC makes nodal lines split into 24 discrete Weyl nodes. Note that the bands along high symmetry lines Γ-M and Γ-L open a gap and some discrete nodes on two $k_z \neq 0$ planes appear as shown in Fig.3S. Base on the Wannier-based tight-binding model, we also found twelve pairs of Weyl points located on the $k_z \neq 0$ planes for both systems.

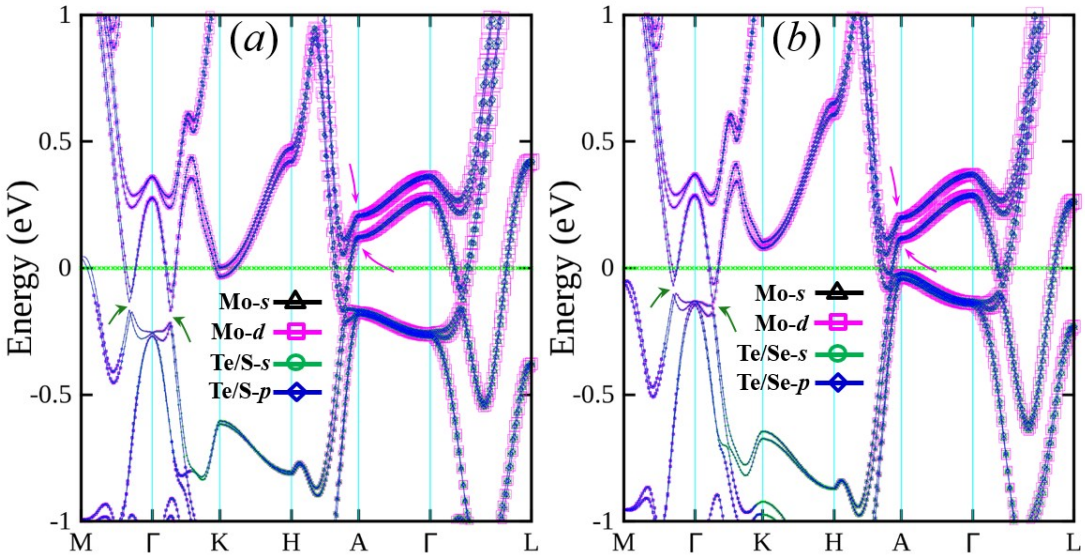

Fig.2S (Color Online). The orbital-resolved bands for (*a*) Mo_2TeS; (*b*) Mo_2TeSe. The green and pink arrows indicate the proximity of Weyl points and four twofold degeneracy points, respectively.

4. Nodal lines and Weyl nodes without and with SOC for Mo_2TeS and Mo_2TeSe

The locations of Weyl nodes for both Mo_2TeS and Mo_2TeSe are also pinpointed using the Wannier-based tight-binding Hamiltonian[9]. These nodal lines and nodes demonstrate similar characteristics of Mo_2SeS in the main text. The nodal lines are located on the mirror symmetry planes which are related by C_3 symmetry. In the presence of SOC, the nodal lines are split into 24 discrete Weyl nodes. There are also similar features with respect to the Weyl node.

Firstly, similar Mo_2SeS, twelve pairs of Weyl nodes can be divided into two groups according to their energies: WP1 and WP2. The energies of half of Weyl nodes are -170meV (-82meV) and other halves are -184meV (-97meV) for Mo_2TeS (Mo_2TeSe). The coordinates of four irreducible Weyl nodes are given in Table 1S.

Second, the 24 Weyl nodes appear roughly in the k_z=±0.32, ±0.34 (Mo_2TeS) and k_z=±0.28, ±0.35×2π/*c* (Mo_2TeSe) planes in the reduced unit, which are symmetric with respect to k_z=0 plane as plotted in Fig.3S (*a*) (*d*). The distribution of 24 Weyl nodes exhibits inversion (time reversal) symmetry c_i, C_{3z} rotation symmetry, and mirror symmetry M_{yz} which is shown clearly in Fig.3S. Utilizing these symmetries, we can deduce the coordinates of all nodes from the coordinates of only four irreducible nodes as given in Table 1S.

Third, similar to Mo_2SeS, the Weyl points are type II Weyl points, which is close to well-known type-II Weyl semimetal, transition metal dichalcogenides and diphosphides MX_2 (M=Mo, W; X=Te, P) consist of 8 type II Weyl nodes [11-14].

Additionally, both Mo_2TeS and Mo_2TeSe have an analogous connection pattern of the Fermi arcs to that of Mo_2SeS.

Table 1S. The locations and energies of four irreducible Weyl nodes for Mo_2TeS and Mo_2TeSe.

Systems	Nodes	k_x(1/Å)	k_y(1/Å)	k_z(1/Å)	Energy(eV)	C_{WP}
Mo_2TeS	wp_1	0.217	0.166	-0.247	-184	-1
	wp_2	0.251	0.105	-0.249	-184	+1
	wp_3	0.289	0.121	0.235	-170	+1
	wp_4	0.249	0.186	0.236	-170	-1
Mo_2TeSe	wp_1	0.174	0.145	-0.251	-82	-1
	wp_2	0.213	0.078	-0.252	-82	+1
	wp_3	0.213	0.186	0.200	-97	-1
	wp_4	0.267	0.090	0.202	-97	+1

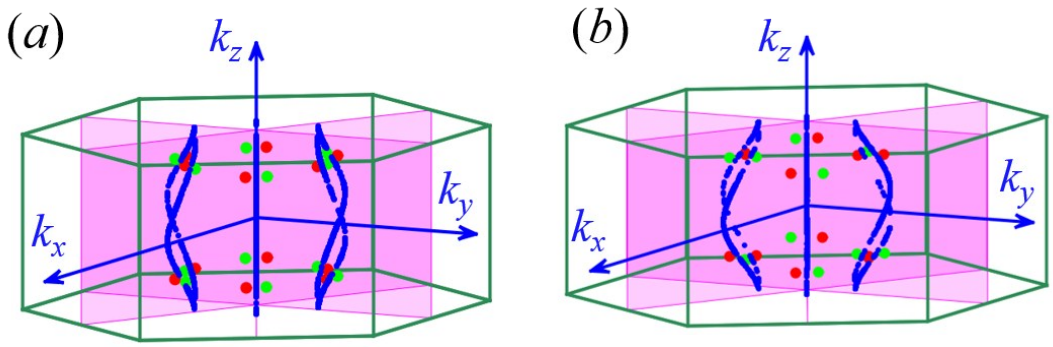

Fig.3S (Color Online). Nodal lines without SOC and Weyl nodes with SOC for (*a*) Mo_2TeS and (*b*) Mo2TeSe. The blue dash lines represent the nodal line. The red and green dots represent the Weyl nodes with positive and negative chirality.

5. Strain effect on the Weyl nodes for Mo_2TeS and Mo_2TeSe.

In the presence of SOC, the locations and energies of Weyl nodes as a function of strain are presented in Fig.4S and Fig.5S. The distribution of all Weyl points with c_i, C_{3z}, and M_{yz} symmetries is analogous to that of strain-free case. The Weyl points move away from the k_z-axis as uniaxial strain varies from -4%(-6%) to 2%(2%) for Mo_2TeS (Mo_2TeSe), whereas the k_z-coordinates close to zero (k_z=0). In contrast, they approach gradually to k_z-axis and their k_z-coordinates close to the k_z=2π/c when biaxial strain changes from -4%(-10%) to 6 %(8%) for Mo_2TeS (Mo_2TeSe). Moreover, the position change of Weyl point is more obvious under biaxial strain than uniaxial strain.

The average energies E_{WP} of Weyl points exhibit similar features to the Mo_2SeS. First, under both types of strain, the variation of E_{WP} demonstrates an opposite change tendency. The E_{WP} increases (decreases) gradually as uniaxial (biaxial) strain from compressive to tensile strain. Second, both Mo_2TeS and Mo_2TeSe are more fragile under the compression than the tensile. The Weyl semimetal state remains just under uniaxial strain range (-4%, 2%) for Mo_2TeS and (-6%, 2%) for Mo_2TeSe. However, both systems show better robustness under biaxial strain. The origin of different

responses may be due to their own structural properties–a layered material usually show an obvious anisotropic response in stacking direction and vertical stacking direction. The maximal separation Δk between Weyl nodes with opposite chirality is the order of magnitude of 0.1Å^{-1} for both Mo_2TeS and Mo_2TeSe as shown in (*c*) of Fig.4S and Fig.5S. The Δk decreases with strain from compression to tensile under uniaxial and biaxial strain for Mo_2TeS and uniaxial for Mo_2TeSe. However, the Δk demonstrates a non-monotonous behavior under biaxial strain for Mo_2TeSe as shown in right bottom panel in Fig.5S. The Δk increases firstly and then decreases when the strain changes from -10% to 8%. The separation Δk is of the order of magnitude 0.2Å^{-1} and reaches the peak around 0.26Å^{-1}/ 0.27Å^{-1} (0.20Å^{-1}/0.20Å^{-1})under uniaxial -4%(-6%)/biaxial -4%(-2%) strain for Mo_2TeS(Mo_2TeSe), respectively.

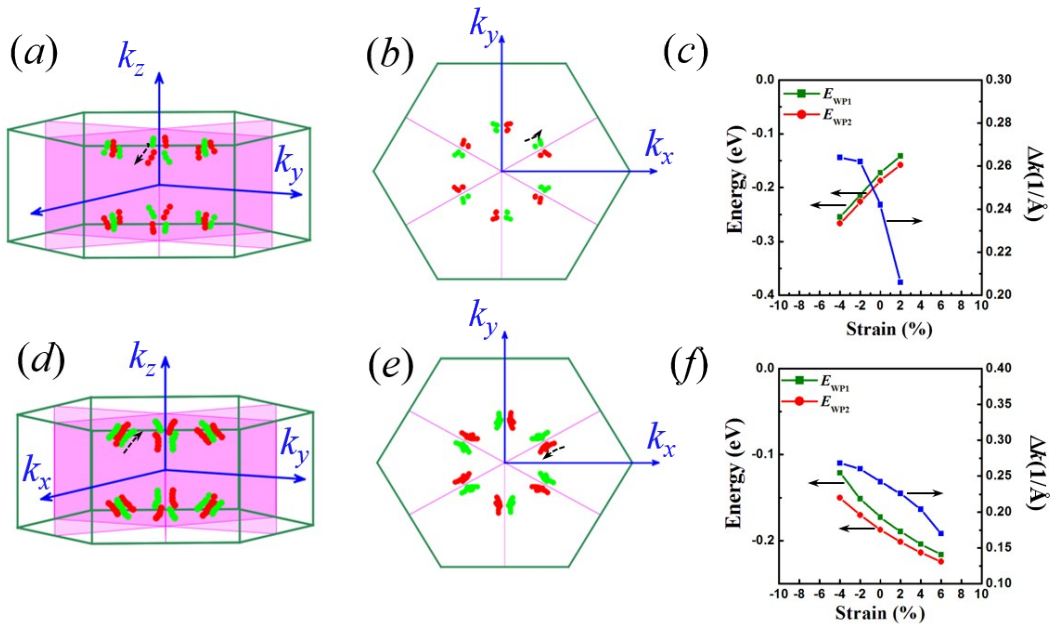

Fig.4S (Color Online).The distribution, energy of Weyl nodes and maximal separation Δk for Mo_2TeS under strain along *c* axis ((*a*) (*b*) (*c*)) and *a*/*b* biaxial ((*d*) (*e*) (*f*)) in the presence of SOC. The red and green dots represent Weyl nodes with positive and negative chirality. The black dash arrow represents the change of strain from compressive to tensile. Here, the BZ corresponds to the BZ of strain-free Mo_2SeS. The blue horizontal dash line represents the Fermi level in (*c*) and (*f*).

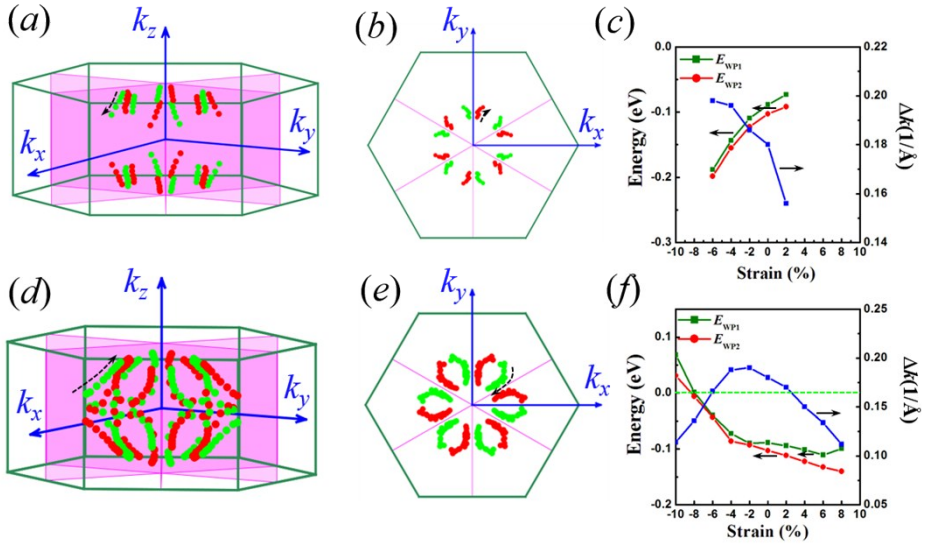

Fig.5S (Color Online).The distribution, energy of Weyl nodes and maximal separation Δk for Mo_2TeSe under strain along *c* axis ((*a*) (*b*) (*c*)) and *a*/*b* biaxial ((*d*) (*e*) (*f*)) in the presence of SOC. The red and green dots represent Weyl nodes with positive and negative chirality. The black dash arrow represents the change of strain from compressive to tensile. Here, the BZ corresponds to the BZ of strain-free Mo_2SeS. The blue horizontal dash line represents the Fermi level in (*c*) and (*f*).

References

1. G. Kresse and J. Furthmu¨ller, *PHYSICAL REVIEW B*, 1996, **54**, 11169.
2. W. Kohn and L. J. Sham, *Physical Review*, 1965, **140**, A1133-A1138.
3. P. Hohenberg and W. Kohn, *Physical Review*, 1964, **136**, B864-B871.
4. H. Gao, Y. Kim, J. W. F. Venderbos, C. L. Kane, E. J. Mele, A. M. Rappe and W. Ren, *Phys Rev Lett*, 2018, **121**, 106404.
5. Z. Wang, Y. Sun, X.-Q. Chen, C. Franchini, G. Xu, H. Weng, X. Dai and Z. Fang, *Physical Review B*, 2012, **85**, 195320.
6. S. Grimme, J. Antony, S. Ehrlich and H. Krieg, *J Chem Phys*, 2010, **132**, 154104.
7. A. Togo and I. Tanaka, *Scripta Materialia*, 2015, **108**, 1-5.
8. A. A. Mostofi, J. R. Yates, G. Pizzi, Y.-S. Lee, I. Souza, D. Vanderbilt and N. Marzari, *Computer Physics Communications*, 2014, **185**, 2309-2310.
9. Q. Wu, S. Zhang, H.-F. Song, M. Troyer and A. A. Soluyanov, *Computer Physics Communications*, 2018, **224**, 405-416.
10. M. P. L. Sancho, J. M. L. Sancho and J. Rubio, *Journal of Physics F: Metal Physics*, 1985, **15**, 851-858.
11. A. A. Soluyanov, D. Gresch, Z. Wang, Q. Wu, M. Troyer, X. Dai and B. A. Bernevig, *Nature*, 2015, **527**, 495-498.
12. Y. Sun, S.-C. Wu, M. N. Ali, C. Felser and B. Yan, *Physical Review B*, 2015, **92**, 161107(R).
13. Z. Wang, D. Gresch, A. A. Soluyanov, W. Xie, S. Kushwaha, X. Dai, M. Troyer, R. J. Cava and B. A. Bernevig, *Phys Rev Lett*, 2016, **117**, 056805.
14. G. Autes, D. Gresch, M. Troyer, A. A. Soluyanov and O. V. Yazyev, *Phys Rev Lett*, 2016, **117**, 066402.